

**EFFECTS OF PDO REGIME ON SUMMER MELT OF
GLACIERS IN THE CASCADES**

by

Carly S. Phelps

A thesis submitted to the Faculty of the University of Delaware in partial fulfillment of the requirements for the degree of Master of Science in Geography

Fall 2012

© 2012 Carly S. Phelps
All Rights Reserved

**EFFECTS OF PDO REGIME ON SUMMER MELT OF
GLACIERS IN THE CASCADES**

by

Carly S. Phelps

Approved: _____

Brian Hanson, Ph.D.

Professor in charge of thesis on behalf of the Advisory Committee

Approved: _____

Tracy DeLiberty, Ph.D.

Chair of the Department of Geography

Approved: _____

Nancy M. Targett, Ph.D.

Dean of the College of Earth, Ocean, and Environment

Approved: _____

Charles G. Riordan, Ph.D.

Vice Provost for Graduate and Professional Education

ACKNOWLEDGMENTS

Thank you to the University of Delaware Department of Geography for providing me with the opportunity, funding, and resources to conduct this research. I would like to thank my advisor, Brian Hanson, for his guidance and support throughout this project. He has been there to share his knowledge, advice, and sense of humor as I completed this research. I would also like to thank my other committee members, Michael O'Neal and Dana Veron, for sharing their expertise. Laura McGowan generously shared her time and experience to help with the setup of WRF, and Tricia Lawston has been there as a source of moral support and assistance while running WRF and analyzing the output. My fellow graduate students have made me feel welcome in the department and provided me with a sense of perspective. Finally, I would like to thank my family and Cale for their love and support.

TABLE OF CONTENTS

LIST OF TABLES	v
LIST OF FIGURES	vi
ABSTRACT	vii
Chapter	
1 INTRODUCTION	1
1.1 Glacier Mass Balance	1
1.2 Climate Forcing	2
1.3 The Pacific Decadal Oscillation	4
1.4 Study Area	5
1.5 Scope of This Study	6
2 METHODS	10
2.1 Experimental Design and Model Setup	10
2.2 The WRF-ARW Model	11
2.2.1 η Coordinates and Vertical Levels	11
2.2.2 Dynamics	12
2.2.3 Physics	13
2.2.4 Initial and Boundary Conditions	13
2.2.5 Nesting	14
3 RESULTS	20
4 DISCUSSION	31
REFERENCES	35

LIST OF TABLES

Table 2.1.	The year and PDO index for the members of each ensemble.	15
Table 2.2.	WRF-ARW physics options used in the simulation.....	17
Table 2.3.	Variables used in WRF-ARW's flux-form Euler equations.	19
Table 3.1.	Average differences (positive minus negative PDO) in each of the boxes in Figure 3.7, as well as the difference in average differences between the two boxes (western box minus eastern box).	30

LIST OF FIGURES

Figure 1.1.	SST (colors), SLP (contours), and wind stress (arrows) anomalies for each phase of the PDO (JISAO, 2000).....	7
Figure 1.2.	August PDO Index obtained from JISAO for years 1900-2011. Years used in the two model ensembles are highlighted.	8
Figure 1.3.	The study area (Google, 2012)	9
Figure 2.1.	The extent of the three model domains.	16
Figure 2.2.	The η coordinate as implemented in WRF-ARW (Shamarock et al, 2008).....	18
Figure 3.1.	Difference (positive PDO - negative PDO) in average surface temperature for the month of August. Significance levels of 90% and above are contoured.....	23
Figure 3.2.	Same as Surface Temperature, but for downward shortwave flux at the ground surface.	24
Figure 3.3.	Same as Surface Temperature, but for downward longwave flux at the ground surface..	25
Figure 3.4.	Same as Surface Temperature, but for upward moisture flux at the ground surface.	26
Figure 3.5.	Same as Surface Temperature, but for top of atmosphere (TOA) outgoing longwave radiation (OLR)	27
Figure 3.6.	Thermal wind difference (positive minus negative PDO), plotted over average 600 hPa temperature for both model ensembles	28
Figure 3.7.	The locations of the two boxes used to investigate differences West and East of the Cascades.	29

ABSTRACT

When interpreting changes in glacier mass balance, it is useful to know which forcings are contributing to the observed changes. One important climate forcing in the Pacific Northwest is the Pacific Decadal Oscillation (PDO). In this study, we investigated whether August PDO phase has an effect on the summer melt of Cascades glaciers using the Weather Research and Forecasting (WRF-ARW) model. We created two ensembles of model runs, one consisting of ten Augusts during which the PDO index was positive, the other consisting of ten Augusts during which the PDO index was negative. All WRF model runs were for the entire month of August. The results indicate that positive PDO summers produce warmer conditions to the west of the Cascades, and cooler, cloudier conditions to the east. Areas east of the Cascades frequently exhibited an opposite response to PDO phase compared to areas west of the Cascades. The magnitudes of the changes due to PDO phase, as well as the magnitudes of the differences in response to PDO phase across the Cascades, are both of a similar magnitude to that expected from modern greenhouse gas forcing. Results also indicate that PDO phase is unlikely to have an effect on the mass balance of Cascades glaciers.

Chapter 1

INTRODUCTION

1.1 Glacier Mass Balance

Understanding glacier mass balance is important because summer melt from glaciers supplies a source of water for irrigation and hydropower in nearby areas, and can also contribute to sea level fluctuations on a century timescale. While the total amount of water stored in glaciers is relatively small compared to the ice sheets on Greenland or Antarctica, many glaciers are in warmer, wetter climates and have smaller response times, making them more vulnerable to climate variability and change (Oerlemans, 2001).

Glacier mass balance measurements have been used as a source of proxy data for determining past climate, as well as an indicator for more recent climate change. Oerlemans (2005) examined 169 glacier records from diverse locations and was able to construct a temperature record completely independent of any other proxy or instrumental data. While many factors affect glacier mass balance, declines in glacier mass are cited as potential indicators of climate change and a contributing factor in sea level rise (IPCC, 2007).

Because no one factor can explain observed changes in glacier mass balance, it is useful to try to determine the contributions from different factors. Some observed glacier mass balance

changes in the Cascades can be attributed to an interplay between local climate variations and glacier geometry (Satinsky, 2009), while others could be due to land-cover induced changes in the surface energy balance (Roth, 2009). Determining the effects of different factors is further complicated by the fact that variation in surface air temperature appears to be dominated by white noise, leading to glacier variations even in a constant climate (Roe and O'Neal, 2009).

In the Pacific Northwest, melt-season temperature variability is highest inland, due to the more continental climate. With the exception of coastal glaciers, glaciers in the Cascades region tend to be more sensitive to changes in melt-season temperature than changes in winter precipitation (Bitz and Battisti, 1999). In addition, interannual variability in melt-season temperature tends to be more uniform over the Cascades region than interannual variability in precipitation (Huybers and Roe, 2009).

1.2 Climate Forcing

Many glaciers in the Cascades are currently experiencing changes in mass balance on a variety of spatial and temporal scales. Annual mass balance measurements, longitudinal profiles, and regional continuity of glacier response all indicate changes in response to climate variation (Pelto, 2006).

CO₂ levels have increased from 280 ppm in the pre-industrial era to 395 ppm in 2012 (ESRL, 2012), with the largest increases happening during the last 10 years. Human activities also have changed several important radiative forcings. The combined radiative forcing from

changes in CO₂, methane, and nitrous oxide is estimated to be +2.30 W m⁻² compared to the pre-industrial era, while the change in aerosol forcing is estimated to be -0.5 W m⁻². Changes in solar radiation since 1750 are estimated to have contributed a radiative forcing of +0.12 W m⁻². (IPCC, 2007). These changes in GHG and radiative forcing accompany an increase in global average temperature and a decline in snow cover and glaciers. Satinsky (2010) found that a component of the behavior of Cascades glaciers could be attributed to this recent warming, though the signal is small and complicated by noise.

Federal forests in the Pacific Northwest were logged extensively until the 1990s, when the Northwest Forest Plan shifted the focus from providing maximum timber yields to providing a sustainable yield while conserving biodiversity and complying with the Endangered Species Act (Thomas et al., 2005). O'Neal et al. (2010) found that a daytime summer temperature difference of 0.7° C could be attributed to 20th century reductions in forest cover. This difference appears to be sufficient to cause glacier mass balance changes.

1.3 The Pacific Decadal Oscillation

Another important factor in Pacific Northwest climate, and the focus of this study, is the Pacific Decadal Oscillation (PDO). The PDO is a pattern of North Pacific sea surface temperature (SST) variability. The PDO has two phases, warm/positive, which dominated from 1977 through the mid-1990s, and cool/negative, which currently dominates after a possible regime shift in the mid-1990s. The “warm” phase of the PDO is characterized by anomalously cool SSTs in the central North Pacific and anomalously warm SSTs along the west coast of the Americas, while the opposite anomalies hold for the “cool” phase (Mantua and Hare, 2001). Figure 1.1 (JISAO, 2000) illustrates the typically SST, SLP, and wind stress anomalies for each phase of the PDO. Typically, one regime will remain dominant for approximately 30 years before a regime shift takes place.

The strength of the PDO is described by the PDO index, defined as the leading PC from an un-rotated EOF analysis of monthly “residual” SSTs poleward of 20N. “Residual” in this case refers to the difference between the observed anomalies and the monthly mean global SST anomalies for the period from 1900-1993 (Mantua and Hare, 2001). A timeseries of August PDO index values from 1900-2011, with years used in this study highlighted, is presented in Figure 1.2.

The PDO is not solely an extra-tropical phenomenon. The PDO has been linked to ENSO via an “atmospheric bridge” (Newman et al., 2003). Anomalous convection induced by ENSO has a widespread influence on atmospheric circulation and surface heat fluxes over the

Pacific, which in turn force SST anomalies that peak a few months after the observed ENSO maximum. Through these ocean-atmosphere interactions, the North Pacific integrates the effects of ENSO over several years, resulting in a reddened ENSO signal.

However, the PDO does not appear to be a phenomenon forced entirely by ENSO or other ocean-atmosphere interactions. The characteristics of the PDO are consistent with noise-forced response where the white noise forcing of the atmosphere is reddened by the ocean as higher-frequency forcings are preferentially damped (Pierce, 2001).

1.4 Study Area

The study area is centered on the Cascades, covering a region from northern California to southern British Columbia. The Cascade Range is located approximately 140 to 200 km inland. Elevations in the Cascades range from about 1,200 to 3,000 m, with isolated peaks at higher elevations such as Mt Rainier at 4,392 m (Western Regional Climate Center, 2012). Figure 1.3 (Google, 2012) shows the topography of the region.

Weather in the area is strongly influenced by oceanic and atmospheric circulation over the Pacific Ocean and the Gulf of Alaska. The region has a strong seasonal precipitation pattern, with approximately two-thirds of the annual precipitation occurring between October and March. Topography also plays a significant role in the weather and climate across the study area. Areas west of the Cascades receive higher annual precipitation than areas to the east. Though the east

is generally drier, a higher proportion of annual precipitation occurs during the warm season (Climate Impacts Group, 2012).

Vegetation varies across the study area from rainforest conditions on the Olympic Peninsula, to stands of Douglas fir, spruce, hemlock, and cedar, to Ponderosa Pine in eastern Washington (Western Regional Climate Center, 2012). Federal forests in the region were logged primarily for a sustainable timber yield prior to the 1990s, when the Northwest Forest Plan was implemented and the focus shifted to maintaining biodiversity and protecting endangered species. Since the 1990s, federal forests in the Pacific Northwest have seen an increase in late-successional and old growth forest (Thomas et al., 2005).

1.5 Scope of This Study

In this study, we aim to determine the role of the PDO in summer melt of glaciers in the Cascades. We used a mesoscale model (the WRF-ARW model, described in Chapter 2), driven by data based on PDO phase. Two model ensembles, one for the positive PDO and one for the negative PDO, were utilized. Because this study is focused on the effects of PDO phase on melt-season temperature, all input data and model runs were for the month of August.

Pacific Decadal Oscillation

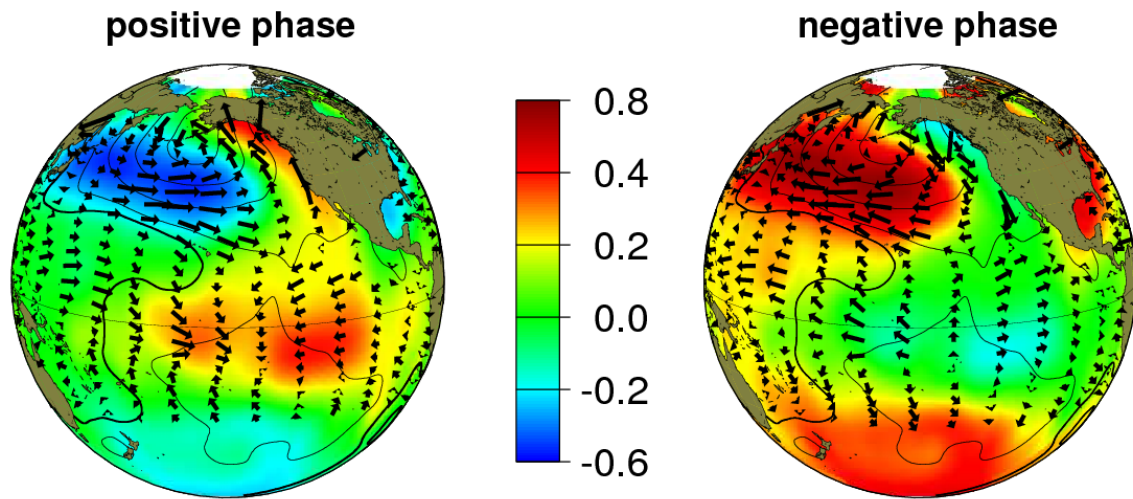


Figure 1.1. SST (colors), SLP (contours), and wind stress (arrows) anomalies for each phase of the PDO (JISAO, 2000). SST anomalies are in °C.

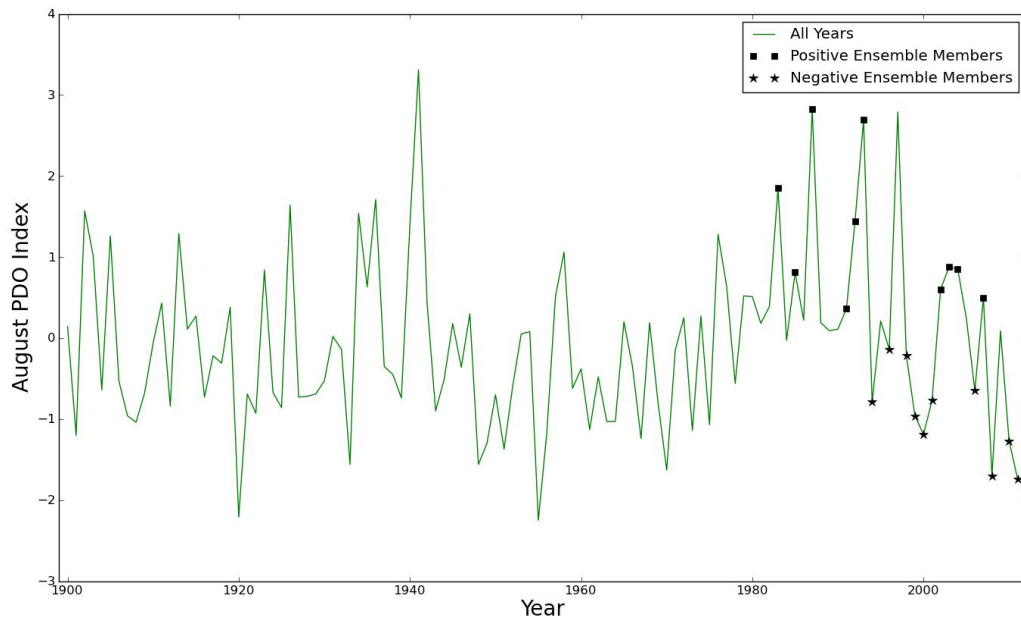


Figure 1.2. August PDO Index obtained from JISAO for years 1900-2011. Years used in the two model ensembles are highlighted.

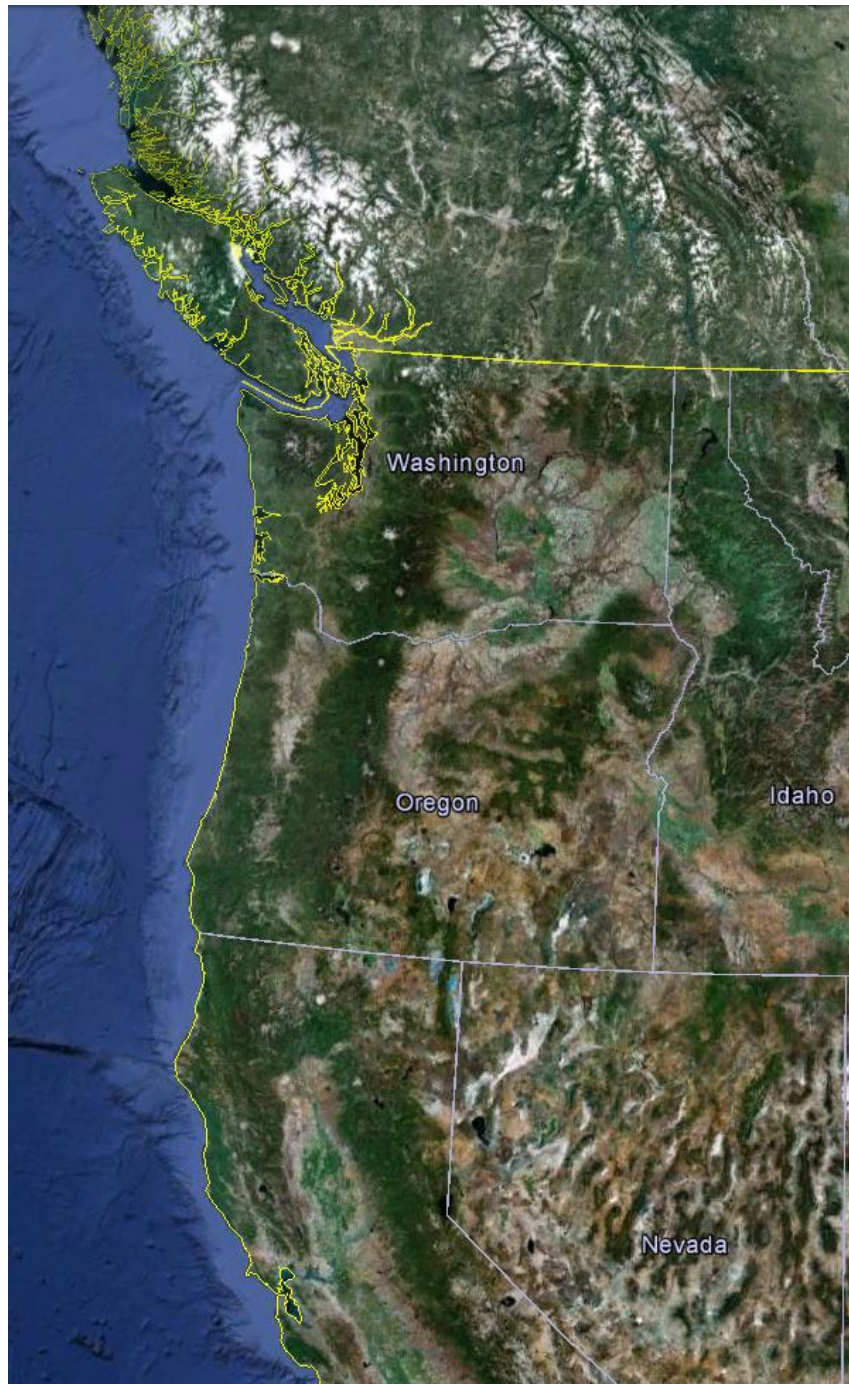


Figure 1.3. The study area: the Pacific Northwest, centered on the Cascade range. Source: "Pacific Northwest." 42° 23' 12.9" N and 118° 32' 4.46" W. **Google Earth.** Copyright 2012 TerraMetrics. 11 Aug 2012.

Chapter 2

METHODS

2.1 Experimental Design and Model Setup

North American Regional Reanalysis (NARR) data were obtained from NCAR as input for the WRF model. NARR data have a spatial resolution of 32 km, data for 30 vertical levels, and a temporal resolution of 3 hours. NARR combines surface and upper-air observations from a variety of sources from 1979-present and assimilates them into one dataset using NCEP's Eta model and Regional Data Assimilation System (Shafran et al., 2005). A more detailed description of this dataset can be obtained from NCEP (2012).

Data covering 20 one-month periods were obtained - ten Augusts with a positive PDO index, and 10 Augusts with a negative PDO index. In order to focus on the effects of melt-season temperature, one ensemble of ten positive PDO Augusts and one ensemble of ten negative PDO Augusts were chosen (Table 2.1). PDO Index values were obtained from the Joint Institute for the Study of the Atmosphere and Ocean (JISAO, 2011). Figure 2.1 shows the August PDO time series for 1900-2011 and where the ensemble members fall.

Our model setup used three domains, with spatial resolutions of 67.5 km, 22.5 km, and 7.5 km. The extent of the domains is shown in Figure 2. All domains ran with a timestep of 180 seconds. Twenty-eight vertical levels were included, with a model top of 100 hPa. Physics

options for all model runs are shown in Table 2.2. All model simulations ran from 00Z on August 1 to 21Z on August 31.

2.2 The WRF-ARW Model

The Weather Research and Forecasting (WRF) Version 3.3 model is a fully compressible, nonhydrostatic model with a hydrostatic option designed for both research and operational numerical weather prediction. For this study, the Advanced Research WRF (ARW) option was used. The ARW dynamics solver uses a terrain-following hydrostatic pressure coordinate to integrate the compressible, non-hydrostatic Euler equations in flux form. Detailed documentation regarding the WRF version 3 model can be found in Shamarock et al. (2008).

2.2.1 η Coordinates and Vertical Levels

WRF uses a terrain-following hydrostatic pressure coordinate, called η , for its vertical coordinate, where η is defined as:

$$\eta = (p_h - p_{ht}) / \mu \quad \text{where } \mu = p_{hs} - p_{ht} \quad (2.1)$$

where p_h is the hydrostatic component of the pressure, p_{ht} is the value along the top boundary, and p_{hs} is the value along the surface boundary.

Figure 2.2 (Shamarock et al, 2008) illustrates the η coordinate as it is implemented in WRF-ARW.

2.2.2 Dynamics

The flux-form Euler equations in WRF-ARW can be written as:

$$\partial_t U + (\nabla \cdot VU) - \partial_x(p\phi_\eta) + \partial_\eta(p\phi_x) = FU \quad (2.2)$$

$$\partial_t V + (\nabla \cdot VV) - \partial_y(p\phi_\eta) + \partial_\eta(p\phi_y) = FV \quad (2.3)$$

$$\partial_t W + (\nabla \cdot VW) - g(\partial_\eta p - \mu) = FW \quad (2.4)$$

$$\partial_t \Theta + (\nabla \cdot V\theta) = F\Theta \quad (2.5)$$

$$\partial_t \mu + (\nabla \cdot V) = 0 \quad (2.6)$$

$$\partial_t \phi + \mu^{-1}[(V \cdot \nabla \phi) - gW] = 0 \quad (2.7)$$

The following diagnostic equation (2.8) and the equation of state (2.9) are also used.

$$\partial_\eta \phi = -\alpha \mu \quad (2.8)$$

$$p = p_0 (R_d \theta / p_0 \alpha)^\gamma \quad (2.9)$$

Table 2.3 lists the variables used in equations 2.2 – 2.9.

2.2.3 Physics

WRF-ARW offers a variety of physics options, which fall into five categories: (1) microphysics, (2) cumulus parameterization, (3) planetary boundary layer, (4) land-surface model, and (5) radiation. The physics packages are separate from the rest of the dynamics solver, and compute tendencies for velocity, potential temperature, and moisture during each model timestep.

2.2.4 Initial and Boundary Conditions

The WRF Preprocessing System (WPS) takes large-scale GriB input data and converts it into a format suitable for use by the ARW solver by using the user-specified domain and resolution. WPS specifies boundary conditions for the outer domain based on the input data, while the outer domains provide boundary conditions for any inner domains. WPS horizontally interpolates input data onto the model domain at the specified resolution for each domain, and vertically interpolates input data onto a number of vertical levels specified by the user.

Because our simulations used real data as input, the initial and boundary conditions are generated from this data by WPS. A lateral boundary condition file is generated that supplies boundary conditions for the beginning of each timestep, as well as a tendency term to move toward the next timestep.

2.2.5 Nesting

Up to three horizontal nested domains of increasing resolution can be utilized, with options for one-way nesting, two-way nesting, or a moving nest. In both one-way and two-way nesting, coarse grid conditions are used to create the fine grid boundary conditions, but in two-way nesting, the fine grid solution replaces the coarse grid solution in locations where the grid points overlap. Our simulations utilize two-way nested runs.

Table 2.1. The year and PDO index for the members of each ensemble.

Positive PDO years		Negative PDO years	
1983	1.85	1994	-0.79
1985	0.81	1996	-0.14
1987	2.83	1998	-0.22
1991	0.36	1999	-0.96
1992	1.44	2000	-1.19
1993	2.69	2001	-0.77
2002	0.6	2006	-0.65
2003	0.88	2008	-1.7
2004	0.85	2010	-1.27
2007	0.5	2011	-1.74

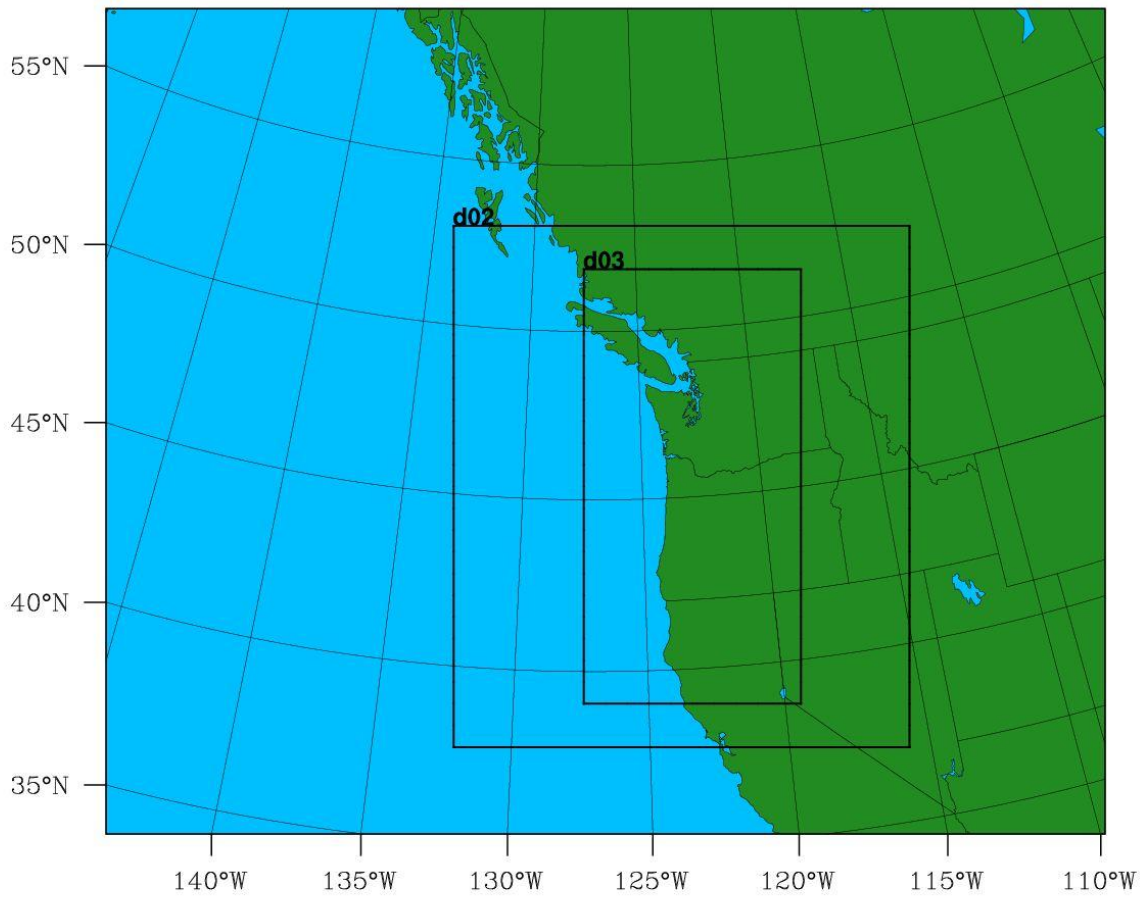


Figure 2.1. The extent of the three model domains.

Table 2.2. WRF-ARW physics options used in the simulation.

Microphysics	WRF Single-Moment 3-class scheme
Cumulus parameterization	Kain-Fritsch scheme
Planetary boundary layer	Yonsei University scheme
Land-surface model	Noah Land Surface Model
Radiation (LW)	Rapid Radiative Transfer Model
Radiation (SW)	Dudhia scheme

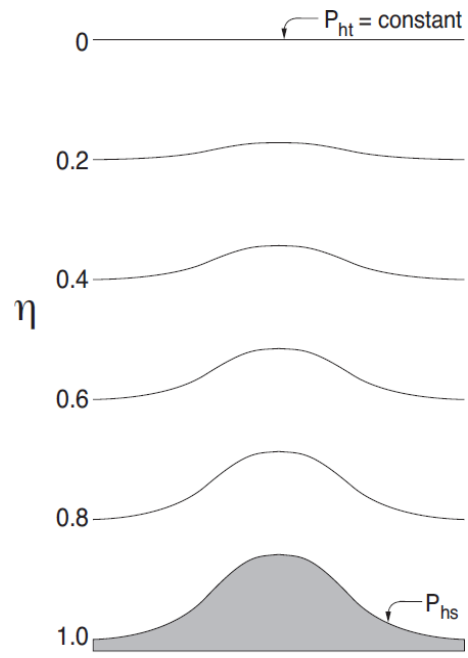


Figure 2.2. The η coordinate as implemented in WRF-ARW (Shamarock et al, 2008).

Table 2.3. Variables used in WRF-ARW's flux-form Euler equations.

$\mathbf{V} = (U, V, W)$	Flux form wind components
$\mathbf{v} = (u, v, w)$	Wind velocity components
ϕ	geopotential
p	pressure
θ	Potential temperature
$\Theta = \mu \theta$	Flux form of potential temperature
$\mu = p_{hs} - p_{ht}$	(See equation 2.1)
$F_U, F_V, F_W,$ and F_Θ	Forcing terms
R_d	Gas constant for dry air
α	Inverse density
γ	Ratio of heat capacities
p_0	Reference pressure (typically 10^5 Pa)

Chapter 3

RESULTS

For each ensemble (positive or negative PDO), an average temperature was calculated for each model gridpoint by averaging over all model timesteps and ensemble members. Average temperature difference maps were then obtained by subtracting the negative PDO ensemble averages from the positive PDO ensemble averages at each gridpoint. Averages and difference maps for downward shortwave flux, downward longwave flux, upward moisture flux, and top-of-atmosphere outgoing longwave radiation (OLR) were all obtained using the same procedure. Contours were added showing areas where differences were significant above the 90% confidence level.

The surface temperature differences show a mode switch in the response to PDO phase along a line roughly corresponding to the crest of the Cascades (Figure 3.1). This same mode switch is also visible in the three surface energy budget plots (shortwave radiation, longwave radiation, and upward moisture flux; Figures 3.2, 3.3, and 3.4 respectively). The mode switch in OLR (Figure 3.5) is located farther west, leaving all of the Cascades area with reduced OLR during positive PDO Augusts compared to negative.

West of the Cascades, surface temperature, downward shortwave flux, and upward moisture flux are increased, while downward longwave flux is decreased. The opposite is true east of the Cascades. These changes are all consistent with the surface temperature changes observed under positive PDO conditions. Reduced surface temperatures east of the Cascades are supported by more incoming longwave radiation being offset by increased cloudiness and decreased incoming shortwave (solar) radiation. Decreased upward moisture flux is also consistent with reduced surface temperatures east of the Cascades, as there will be less energy available for evaporation.

In order to explore the differences in upper-air circulation between PDO regimes, the difference in average August thermal wind between the positive and negative ensembles was calculated. For this purpose, thermal wind was defined as the average geostrophic wind at 500 hPa minus the average geostrophic wind at 700 hPa. The difference in thermal wind (positive minus negative PDO) is shown in Figure 6. The arrows indicate the magnitude and direction of the change in the thermal wind, with larger arrows indicating a larger difference. Contours on Figure 6 indicate the average 600 hPa temperature across all runs from both ensembles.

Areas of cold and warm air advection can be seen in Figure 6 by examining the relationship between the temperature contours and the thermal wind difference arrows. Areas where large arrows are perpendicular to the temperature contours indicate areas of strongest temperature advection, and if the arrows are blowing from cooler toward warmer temperatures,

this indicates an increase in cold air advection during positive PDO Augusts. Thermal wind differences indicate increased cold air advection east of the Cascades during the positive PDO, with little cold air advection west of the Cascades. These changes in the thermal wind provide a dynamical explanation for the surface difference maps by illustrating changes in the upper-air circulation during positive PDO conditions.

To further examine the mode switch across the Cascades, differences between two characteristic regions, one east of the Cascades and one west of the Cascades, were examined. The extent of the two boxes encompassing these regions is shown in Figure 3.7. The two boxes were chosen based on areas with statistically significant differences, giving priority to areas of significant surface temperature differences since surface temperature has the most direct relationship to glacier melt.

Average differences (positive minus negative PDO) in surface temperature and energy budget variables were computed for each box, as well as the difference between the two boxes (western box minus eastern box). These differences are shown in Table 3.1. In order to make better comparisons between the different variables, average differences for latent heat flux (which has units of Watts per square meter and can more easily be compared with the other energy budget variables) were computed as a complement to the upward moisture flux values. Surface temperature, incoming SW radiation, and latent heat flux have the most notable differences between the two boxes, partly due to the fact that the sign of the differences changes when moving from west to east. This supports the areas of statistically significant differences on the difference maps for surface temperature and incoming SW radiation (Figures 3.1 and 3.2, respectively).

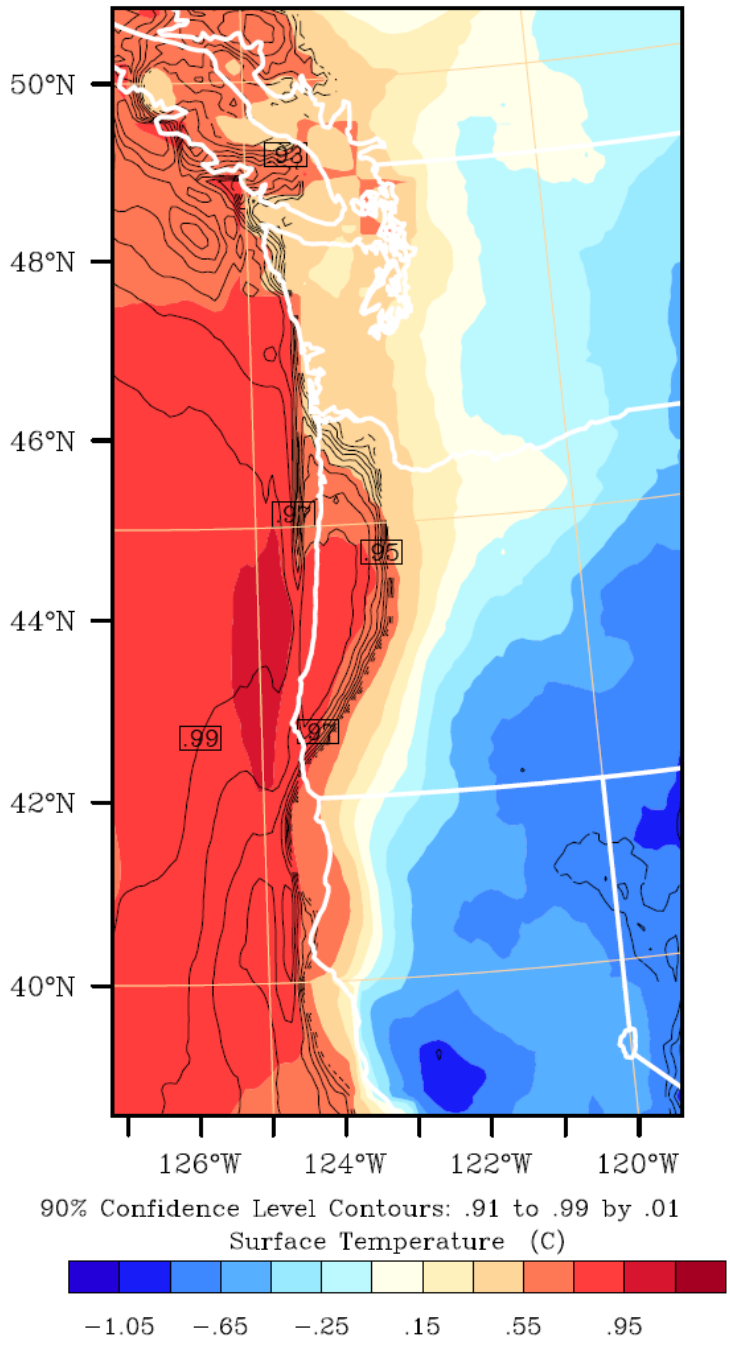


Figure 3.1. Difference (positive PDO - negative PDO) in average surface temperature for the month of August. Significance levels of 90% and above are contoured. Significant temperature differences occur mainly offshore and along the coast. Because the PDO is based on SST variations, this is expected. A shift from positive to negative differences is visible along a line roughly corresponding to the crest of the Cascades.

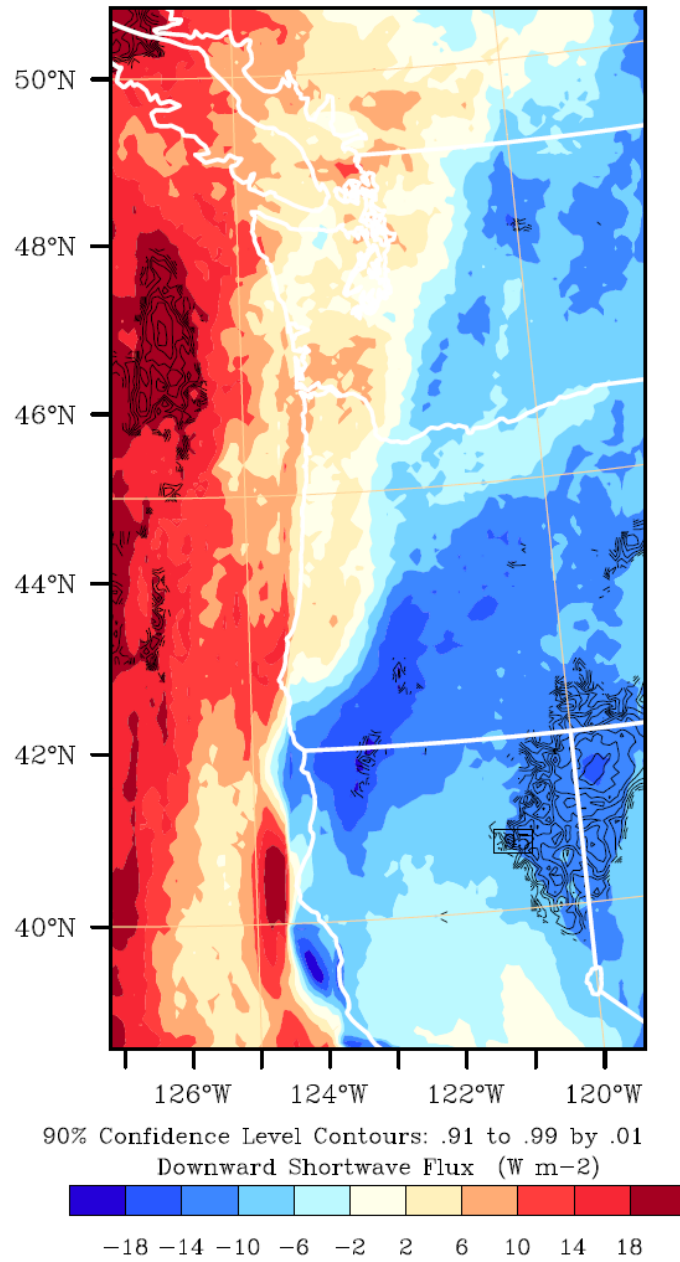


Figure 3.2. Same as Surface Temperature, but for downward shortwave flux at the ground surface. A similar mode switch in the sign of the differences across the Cascades is apparent. The higher spatial variability (compared to surface temperature difference) indicates the role of surface cover variation on albedo.

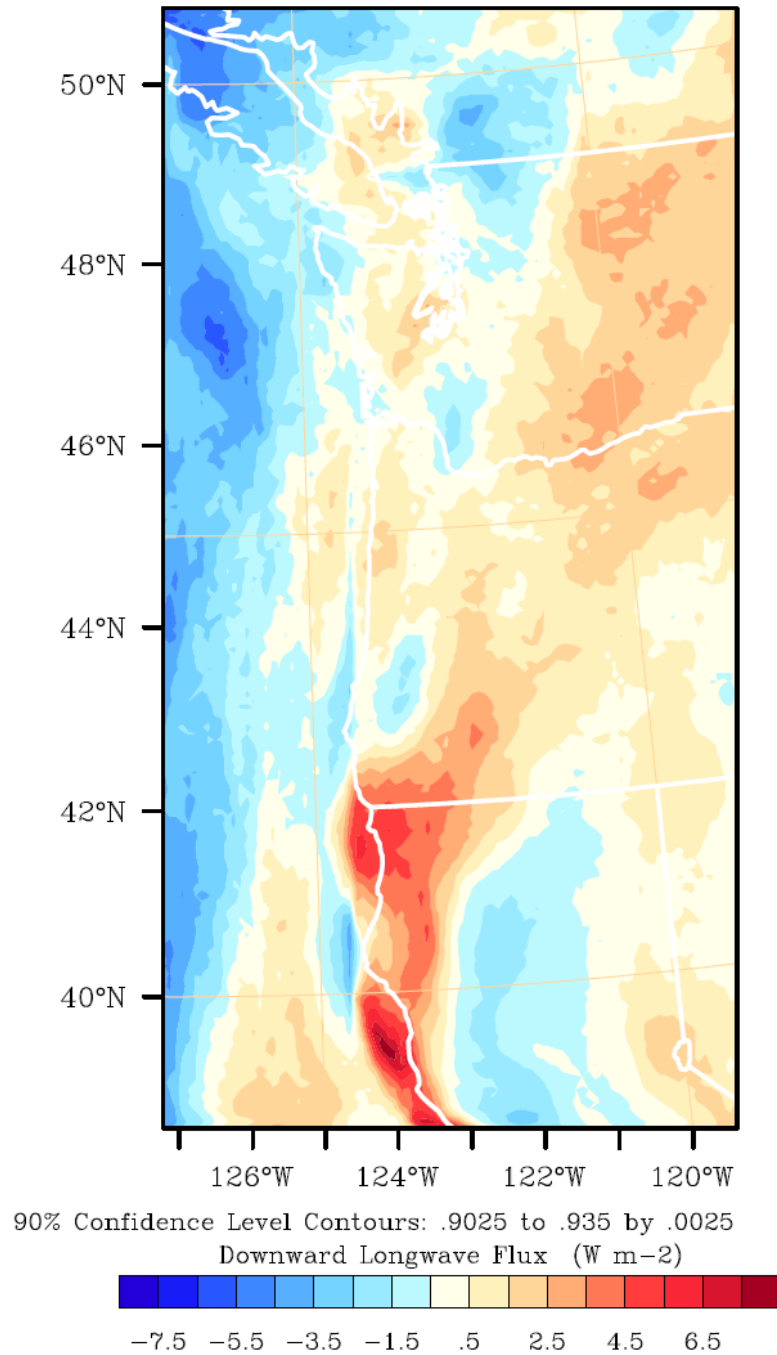


Figure 3.3. Same as Surface Temperature, but for downward longwave flux at the ground surface. The magnitude of the differences is smaller than that of shortwave radiation, and none of the differences are significant, but a similar pattern can still be observed. Differences are generally of the opposite sign as downward shortwave flux.

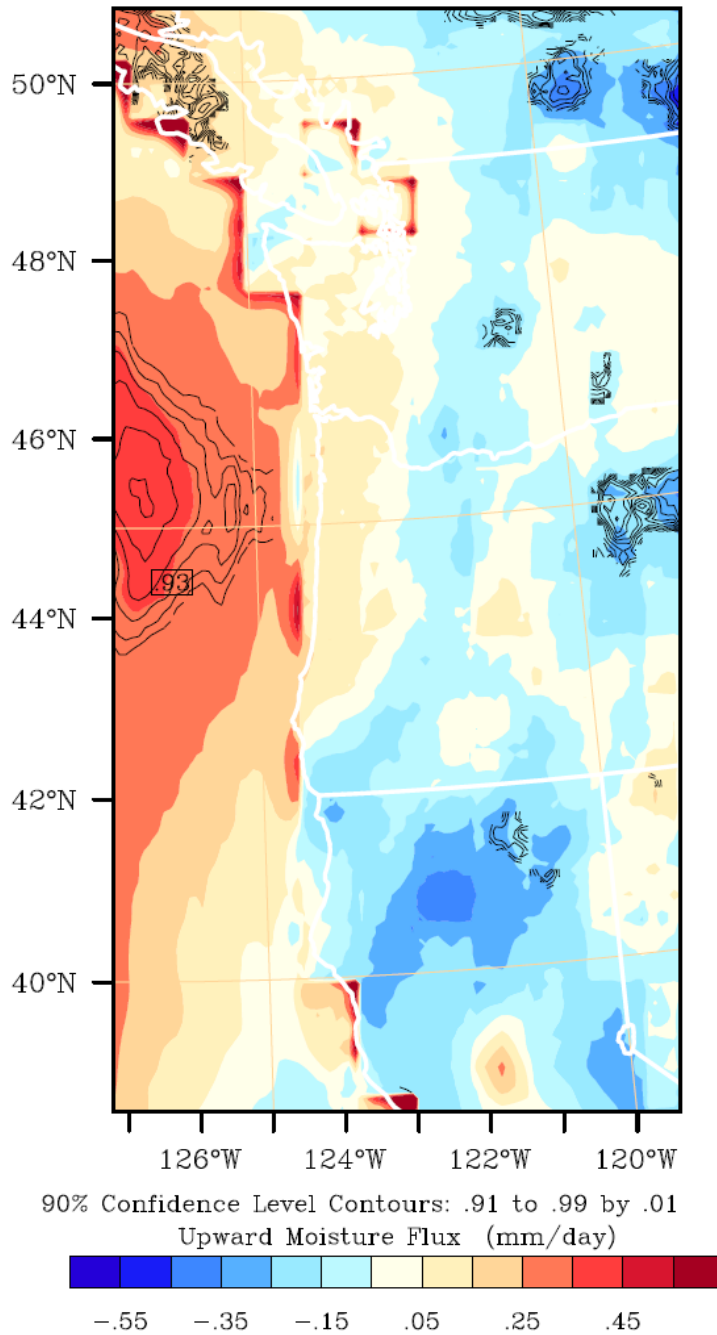


Figure 3.4. Same as Surface Temperature, but for upward moisture flux at the ground surface. The mode switch is less readily apparent for moisture than for temperature and radiation.

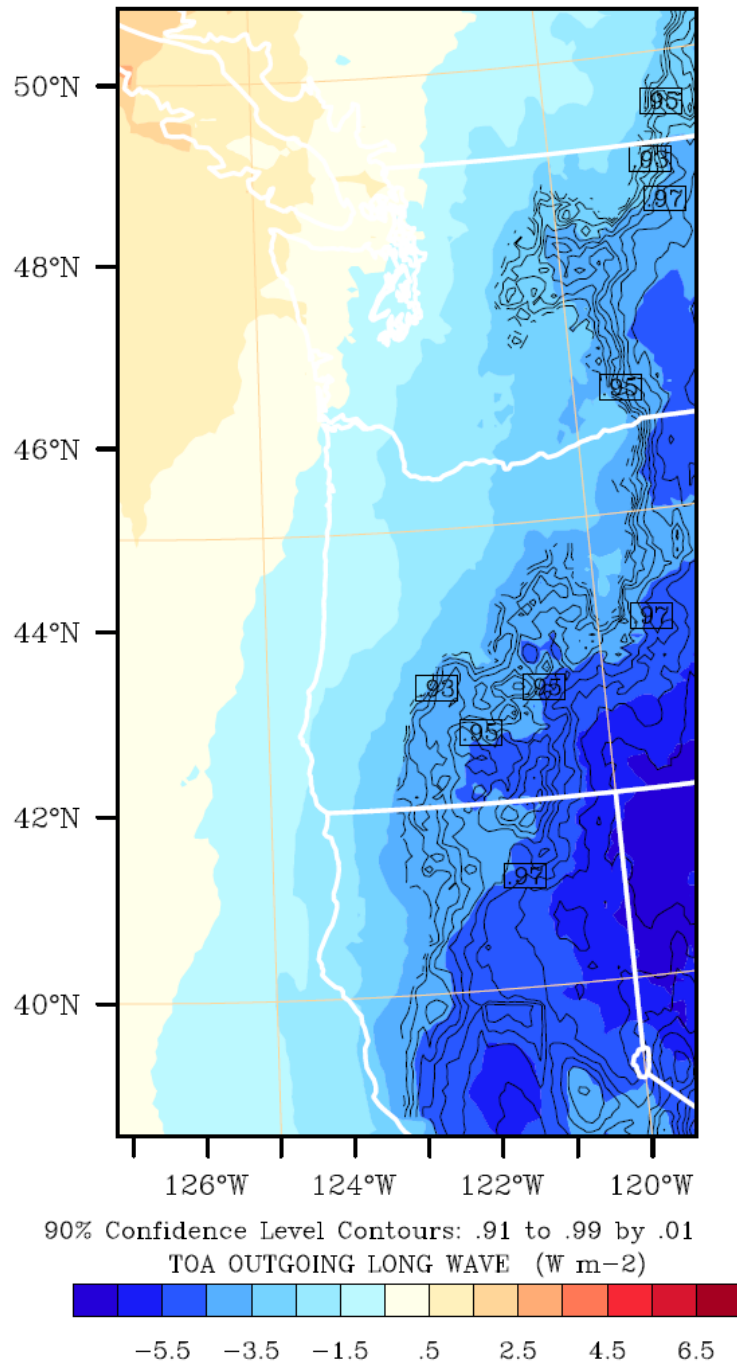


Figure 3.5. Same as Surface Temperature, but for top of atmosphere (TOA) outgoing longwave radiation (OLR). While there is a decrease in OLR across most of the domain, statistically significant decreases in OLR are mainly found east of the Cascades.

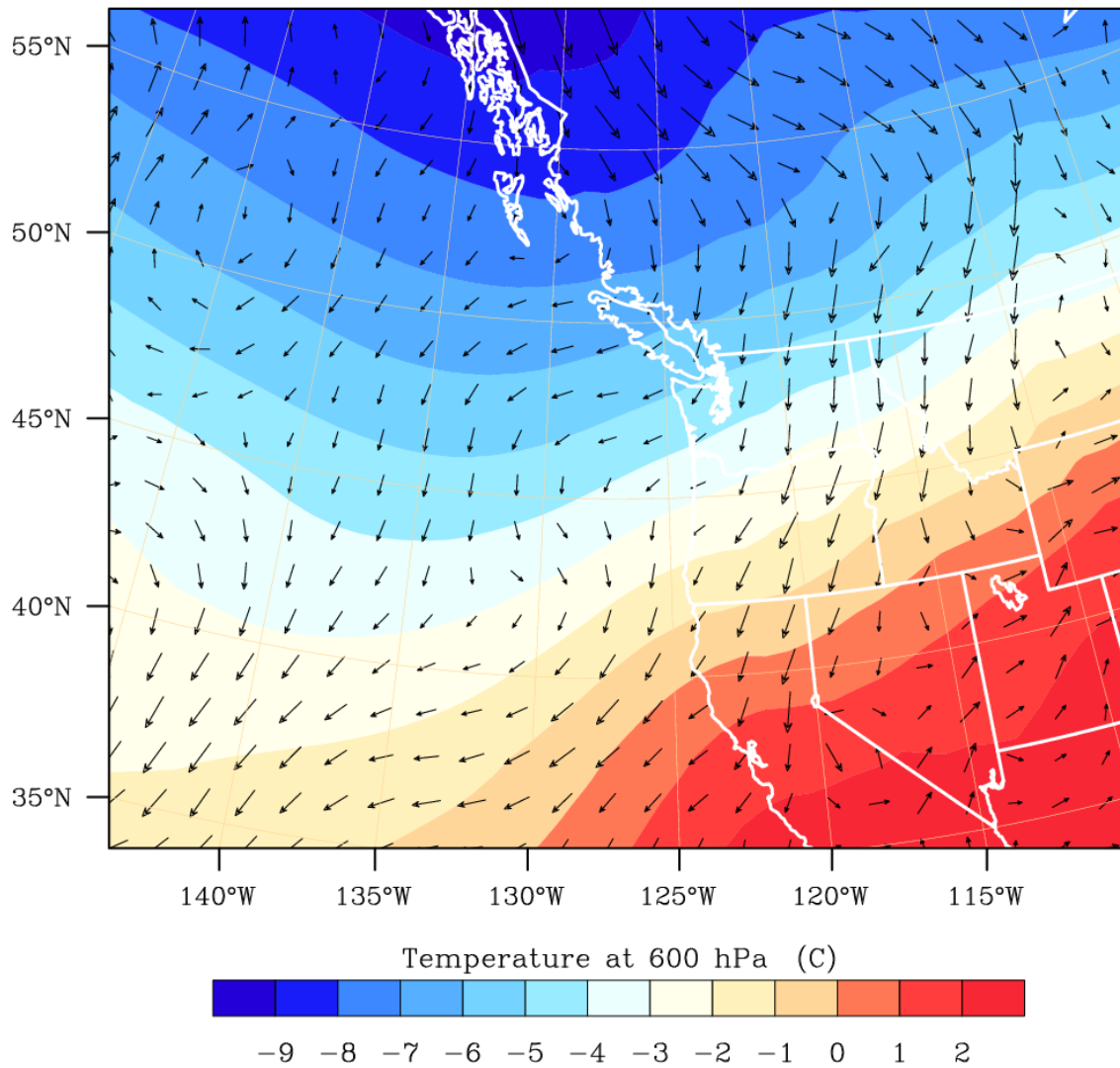


Figure 3.6. Thermal wind difference (positive minus negative PDO), plotted over average 600 hPa temperature for both model ensembles. Thermal wind was calculated as the difference between the 500 hPa and 700 hPa geostrophic wind. Areas of cold air advection correspond to areas of decreased surface temperature east of the Cascades.

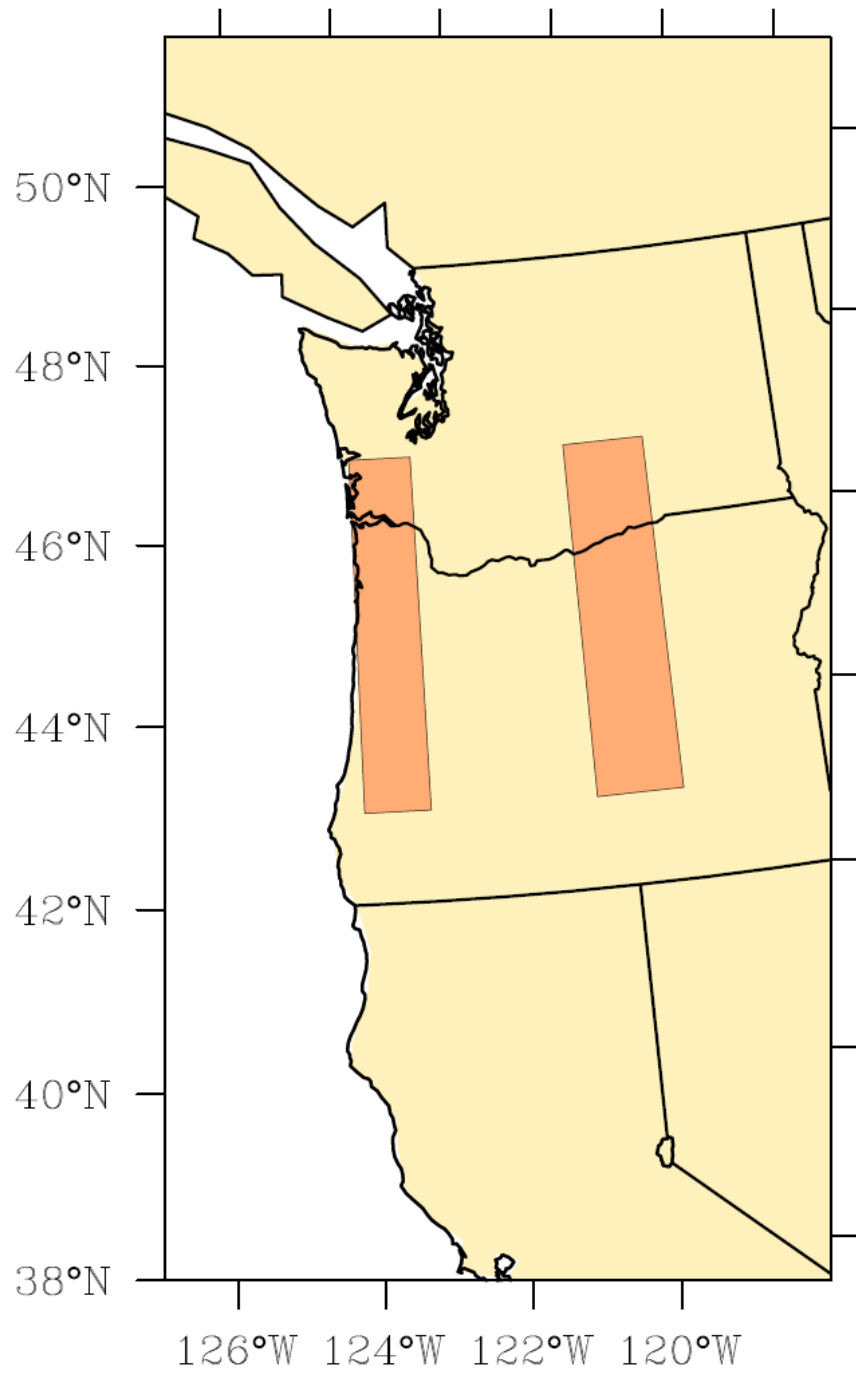


Figure 3.7. The locations of the two boxes used to investigate differences West and East of the Cascades.

Table 3.1. Average differences (positive minus negative PDO) in each of the boxes in Figure 3.7, as well as the difference in average differences between the two boxes (western box minus eastern box).

Variable	Average difference in western box	Average difference in eastern box	Difference between avg differences (W - E)
Sfc Temp (°C)	0.6	-0.4	1.0
Incoming SW (W m ⁻²)	2.9	-9.2	12.1
Incoming LW (W m ⁻²)	0.3	1.3	-1.0
Upward Moisture Flux (mm/day)	0.07	-0.11	0.18
Latent Heat Flux (W m ⁻²)	1.9	-3.1	5.0
OLR (W m ⁻²)	-1.4	-4.2	2.8

Chapter 4

DISCUSSION

The mode switch over the Cascades visible in the surface energy budget difference maps was an interesting and unexpected result. A coherent pattern is visible on the difference maps for surface temperature and the surface radiation components. In each case, the sign of the differences changes along a line roughly corresponding to the crest of the Cascades. The pattern is weak in some cases, with only small areas of statistically significant differences, but the fact that it occurs across several different surface variables is noteworthy. The weakness of the pattern at the 90% significance level could also be due to the relatively small sample size (ten ensemble members for each PDO phase), a number that was constrained by the time and computing resources available for model runs, as well as by suitable available input data. In the case of surface temperature, most statistically significant differences are over or near the ocean – a result that is expected since the PDO index is based on SSTs. However, the mode switch on these difference maps shows that the effects of the PDO are not limited to marine and coastal areas, but instead extend far inland and produce responses different from those expected on the coast. The effect of the mode switch is illustrated by the fact that the differences between two characteristic regions west and east of the Cascades are of approximately the same magnitude as the differences between PDO phases inside each region (Table 3.1).

In general, shortwave radiation and longwave radiation have opposite responses, indicating that PDO phase has an effect on the type of incoming radiation to the ground surface in many parts of the Pacific Northwest. A decrease in downward shortwave radiation paired with an increase in downward longwave radiation in eastern Washington and Oregon could indicate an increase in cloudiness in these areas during positive PDO Augusts. This increase in cloudiness is further supported by the differences in incoming SW radiation between the boxes east and west of the Cascades (Table 3.1).

Of all the difference maps, upward moisture flux has the least coherent pattern and the least obvious mode switch. Several areas in eastern Washington and Oregon exhibit the “opposite” sign than would be expected if they were strictly following the mode switch. However, areas exhibiting the “opposite” sign (areas of increased upward moisture flux in eastern Washington and Oregon during the positive PDO) are almost entirely composed of small differences that are not statistically significant. While upward moisture flux did not clearly follow the mode switch, the difference in the latent heat flux between the two characteristic regions (Table 3.1) was relatively large at 5.0 W m^{-2} .

While the mode switch is evident in the maps of all surface energy budget components, the OLR map clearly does not follow the same mode switch. Instead, nearly all of the Pacific Northwest experiences a decrease in OLR during the positive PDO phase.

The OLR difference map also indicates an increase in cloudiness over eastern Washington and Oregon. The decrease in top-of-atmosphere OLR is consistent with overall

cooler temperatures and higher cloud tops. While nearly the entire Pacific Northwest experiences a decrease in OLR during the positive phase of the PDO, it is worth noting that all areas with statistically significant decreases are located east of the Cascades. These significant differences in OLR provide stronger evidence for an increase in cloudiness than incoming shortwave and longwave radiation, since neither incoming radiation component had large areas of statistically significant differences in the areas of interest.

The cooling east of the Cascades in response to positive PDO phase can also be connected to upper-air patterns. The 500 to 700 hPa thermal wind difference indicates cold air advection in that layer, adding another dimension to the story told by the surface radiation and OLR differences and providing a dynamical link between the surface and upper-air variables.

In summary, the effects of PDO regime appear to change in sign when crossing a line roughly corresponding to the crest of the Cascades. This mode switch is especially noteworthy because the magnitudes of the differences across the Cascades are of a similar magnitude as the changes between PDO phases. Positive PDO Augusts appear to produce cooler, drier conditions over much of eastern Washington and Oregon through an increase in cloudiness, a decrease in incoming shortwave radiation, and an increase in cold air advection due to changes in upper-air circulation. Because differences in temperature and energy budget components directly over the Cascades were small, and no differences in this area were significant, it is unlikely that PDO regime affects the summer melt of Cascades glaciers. Observed changes in glacier mass balance are likely due to land cover changes (Roth, 2009), global warming (Satinsky, 2009), and the influence of atmospheric white noise or short-term “weather” (Roe and O’Neal, 2009).

While PDO phase in the Pacific Northwest is most frequently associated with its effects on ocean temperatures and fisheries production (Mantua et al, 1997), the mode switch across the Cascades, combined with statistically significant differences in surface energy budget variables east of the Cascades, indicates that the effects of the PDO are not limited to coastal and marine areas.

REFERENCES

About Pacific Northwest Climate. Climate Impacts Group.
<http://cses.washington.edu/cig/pnwc/pnwc.shtml>

Bitz, C. M. and Battisti, D. S. (1999). Interannual to Decadal Variability in Climate and Glacier Mass Balance in Washington, Western Canada, and Alaska. *Journal of Climate* **12**, 3181-3196.

Climate of Washington. Western Regional Climate Center.
<http://www.wrcc.dri.edu/narratives/WASHINGTON.htm>

Google Inc. (2012). Google Earth (Version 5.1.3533.1731) [Software]. Available from
<http://www.google.com/earth/download/ge/>

Huybers, K. and Roe, G.H. (2009). Spatial Patterns of Glaciers in Response to Spatial Patterns in Regional Climate. *Journal of Climate* **22**, 4606-4620.

IPCC, 2007: Summary for Policymakers. In: *Climate Change 2007: The Physical Science Basis. Contribution of Working Group I to the Fourth Assessment Report of the Intergovernmental Panel on Climate Change* [Solomon, S., D. Qin, M. Manning, Z. Chen, M. Marquis, K.B. Averyt, M. Tignor and H.L. Miller (eds.)]. Cambridge University Press, Cambridge, United Kingdom and New York, NY, USA.

Mantua, N.J., Hare, S.R., Zhang, Y., Wallace, J.M., and Francis, R.C. (1997). A Pacific Interdecadal Climate Oscillation with Impacts on Salmon Production. *Bulletin of the American Meteorological Society* **78**, 1069-1078.

Mantua, N. J. and Hare, S. R. (2001). The Pacific Decadal Oscillation. *Journal of Oceanography* **58**, 35-44.

The North American Regional Reanalysis (NARR) Archive at NCAR. National Center for Atmospheric Research, Boulder, CO. <http://rda.ucar.edu/pub/narr/>

Newman, M., Compo, G.P., and Alexander, M.A. (2003). ENSO-Forced Variability of the Pacific Decadal Oscillation. *Journal of Climate* **16**, 3853-3857.

Oerlemans, J. (2005). Extracting a climate signal from 169 glacier records. *Science* **308**, 675-677.

Oerlemans, J. (2001). "Glaciers and Climate Change." Swets and Zetlinger.

O'Neal, M.A., Roth, L.B., Hanson, B., and Leathers, D.J. (2010). A Field-Based Model of the Effects of Landcover Chnages on Daytime Summer Temperatures in the North Cascades. *Physical Geography* **31**, 137-155

Pacific Decadal Oscillation Graphics. Joint Institute for the Study of the Atmosphere and Ocean. University of Washington, Seattle, WA. http://jisao.washington.edu/pdo/img/pdo_warm_cool.ps

"Pacific Northwest." 42 23 12.9 N and 118 32 4046 W. Google Earth. Copyright 2012 TerraMetrics. 11 Aug 2012.

PDO Index. Joint Institute for the Study of the Atmosphere and Ocean. University of Washington, Seattle, WA. <http://jisao.washington.edu/pdo/PDO.latest>

Pelto, M. (2006). The current disequilibrium of North Cascade glaciers. *Hydrological Processes* **20**, 769-779.

Pierce, D.W. (2001). Distinguishing coupled ocean-atmosphere interactions from background noise in the North Pacific. *Progress in Oceanography* **49**, 331-352.

Recent Mauna Loa CO₂. NOAA Earth System Research Laboratory.
<http://www.esrl.noaa.gov/gmd/ccgg/trends/>

Roe, G.H. and O'Neal, M.A. (2009). The response of glaciers to intrinsic climate variability: observations and model of late-Holocene variations in the Pacific Northwest. *Journal of Glaciology* **55**, 839-854.

Roth, L. B. (2009). "Modeling Landcover-Induced Increases in Daytime Summer Temperatures Near Mount Adams, Washington." University of Delaware.

Satinsky, A. M. (2009). "Geometric Changes of 742 North Cascade Glaciers Derived from 1958 and 2006 Aerial Imagery." University of Delaware.

Shafran, P., Woollen, J., Ebisuzaki, W., Shi, W., Fan, Y., Grumbine, R., and Fennessy, M. Observational Data Used for Assimilation in the NCEP North American Regional Reanalysis. 85th AMS Annual Meeting, San Diego, CA. 11 Jan 2005. Conference Presentation.

Shamarock, W.C., Klemp, J.B., Dudhia, J., Gill, D.O., Barker, D.M., Duda, M.G., Huang, X., Wang, W., and Powers, J.G. (2008). A Description of the Advanced Research WRF Version 3. National Center for Atmospheric Research, Boulder, CO.

Thomas, J.W., Franklin, J. F., Gordon, J. and Johnson, K.N. (2005). The Northwest Forest Plan: Origins, Components, Implementation Experience, and Suggestions for Change. *Conservation Biology* **20**, 277-287.